

Numerical Simulations of a Gravity Wave Event over CCOPE. Part II: Waves Generated by an Orographic Density Current

FUQING ZHANG AND STEVEN E. KOCH

Department of Marine, Earth and Atmospheric Sciences, North Carolina State University, Raleigh, North Carolina

(Manuscript received 3 March 1999, in final form 26 August 1999)

ABSTRACT

A mesoscale numerical model and detailed observations are used to investigate the generation and maintenance of a mesoscale gravity wave event observed in eastern Montana on 11 July 1981 during the Cooperative Convective Precipitation Experiment (CCOPE). It is shown that the interaction between an orographic density current and a mountain barrier leads to the generation of the gravity waves.

The simulation results suggest the following four-stage conceptual model. During stage I, shortly after sunset, the remnant up-branch of a thermally driven upslope flow east of the Rockies was driven back toward the mountain by the pressure gradient force associated with a cool pool over North Dakota. The nocturnal stable layer over eastern Montana was strengthened during passage of this density current. During the 1–2-h transition period of stage II, the advancing density current became blocked as it encountered the higher terrain. An isentropic ridge developed above the original warm lee trough due to strong adiabatic cooling caused by the sustained upward motion in the presence of orographic blocking. During stage III, an even stronger upward motion center formed to the east of the density current head updraft in response to an eastward horizontal pressure gradient force produced by the isentropic ridge. In stage IV, as the density current head collapsed and downward motion developed to the west of the original updraft in quadrature phase with the isentropic perturbation, a gravity wave was generated. This wave propagated eastward with the mean wind (opposite to the motion of the earlier density current) and was maintained by the strong wave duct established earlier by the density current. Thus, the mountain–plains circulation may at times generate mesoscale gravity waves (and deep convection) hours after diurnal heating has ended.

1. Introduction

Mesoscale gravity waves with wavelengths of 50–500 km and periods of 1–4 h can create important effects on the weather (Uccellini and Koch 1987; Koch and O’Handley 1997). Until recently, many previous studies of these phenomena relied exclusively upon observational analyses. Since the pioneering numerical study of a large-amplitude gravity wave event by Powers and Reed (1993), mesoscale numerical models have developed into powerful tools for the study of gravity wave structure, generation, and maintenance mechanisms, all of which are difficult to determine with standard observations (Powers 1997; Pokrandt et al. 1996; Kaplan et al. 1997; Koch and O’Handley 1997).

The following generation mechanisms for mesoscale gravity waves have been proposed: convection, density impulses, cross-frontal ageostrophic accelerations, shear instability, geostrophic adjustment related to jet/frontal

systems or to sources of diabatic heating, and topographic forcing (Gossard and Hooke 1975). The theory for terrain forcing of stationary mountain waves and lee waves is rather well developed; however, orography has not generally been suggested to be an important source of *propagating* mesoscale gravity waves, nor are the dynamics of these phenomena well understood.

Numerous investigations have shown that during the daytime, as the air adjacent to the mountain slopes becomes warmer than the air in the free atmosphere at the same height above the surrounding valley, a horizontal pressure gradient force is created at low levels directed from the valley to the mountains. This force causes the near-surface air from the valley to flow up the mountain, while a reversed pressure gradient forces an upper-level return flow in the opposite direction (Atkinson 1981; Banta 1984; Bossert and Cotton 1994a,b). Banta (1986) used a nonhydrostatic numerical model to perform a 2D simulation of a mountain–valley circulation. This study confirmed that the pressure–gradient force is the primary mechanism for generating the thermally driven, upslope wind. He pointed out that with relatively strong winds at the mountain ridge top, the subsequent transition to downslope flow occurred as downslope winds first mixed downward and then advected horizontally away

Corresponding author address: Fuqing Zhang, Department of Marine, Earth and Atmospheric Sciences, Campus Box 8208, North Carolina State University, Raleigh, NC 27695-8208.
E-mail: fzhang@ucar.edu

from the mountains, just as revealed by observational studies (Banta 1984).

Numerical investigations also have been performed of a regional-scale circulation termed the mountain–plains solenoid (MPS). Tripoli and Cotton (1989a) used a numerical model with fully explicit microphysics to study the interaction between the MPS circulation, which occurs on a broader scale than that of a mountain–valley circulation, and the growth of a mesoscale convective complex (MCC). Of particular interest to the current study is their finding that the up-branch of the deep MPS broke down in the late afternoon into a train of propagating gravity waves, and that these waves organized the convection into an MCC downwind of the mountains later at night.

Wolyn and McKee (1994) presented a conceptual model of the evolving daytime mountain–plain circulation east of a 2-km-high and 60-km-wide barrier. Their model is composed of a sunrise state followed by three

distinct phases as shown in Fig. 1. The sunrise state consists of the complex interaction between nocturnal katabatic and ambient flows. Phase 1 results from the weakening of the nocturnal flow as it interacts with the daytime heating. This phase lasts until 3–4 h after sunrise. Phase 2 is defined by the developing MPS and may last until sunset. Phase 3 is characterized by the eastward migration of this solenoid (this may not happen on all days). The authors pointed out that the migrating solenoid itself is a disturbance that can significantly affect the atmosphere over the eastern plains. The MPS described here has a much larger scale compared to the local leeside circulation of the Rockies studied by Banta (1986).

Bossert and Cotton (1994a,b) identified the up-branch of the daytime MPS as a westward-propagating density current (WPDC) based upon a 3D simulation. The conceptual model they proposed is discussed in detail in section 4a. Bischoff-Gauss et al. (1989) found that the

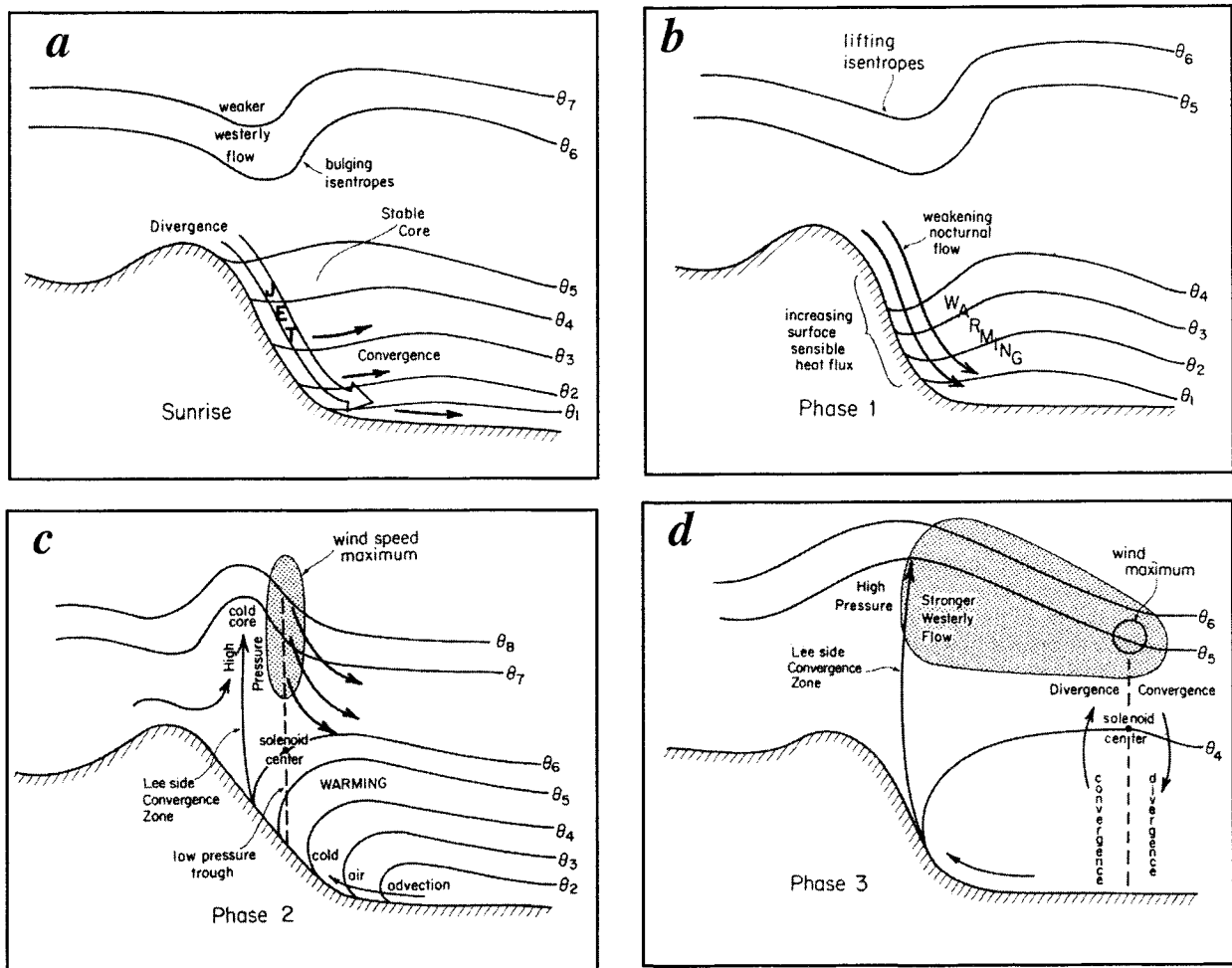


FIG. 1. Conceptual daytime MPS circulation model after Wolyn and McKee (1994): (a) sunrise state, in which there is an interaction between nocturnal thermal and ambient flows; (b) phase 1, during which the weakening nocturnal flow interacts with surface heating; (c) phase 2, consisting of the developing solenoid; and (d) phase 3, the migrating solenoid. The various features shown in the schematic model are discussed in the text.

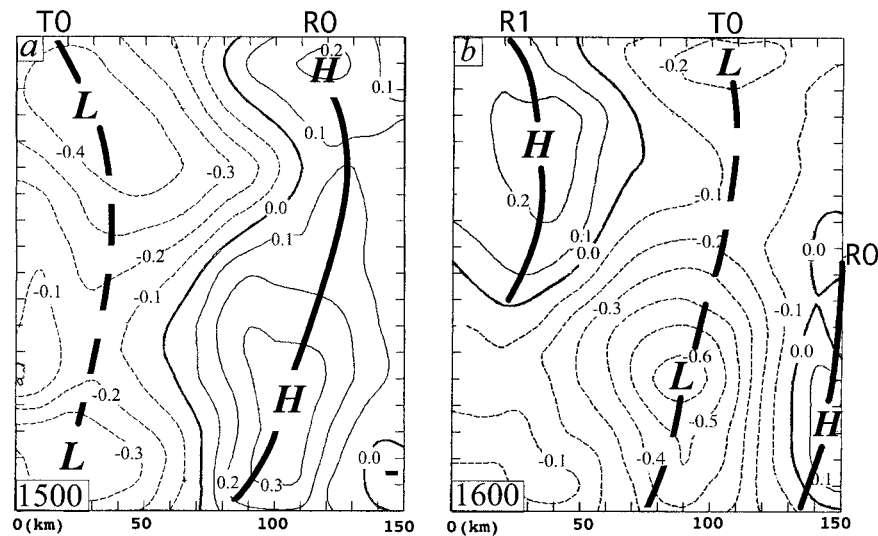


FIG. 2. Objectively analyzed surface pressure perturbation fields (Koch et al. 1988) depicting the primary wave mode over the CCOPE mesonet network (Fig. 3a) at (a) 1500 and (b) 1600 UTC 11 Jul 1981 ($\Delta = 0.1$ hPa). Gravity wave crests R0 and R1 and wave trough TO are depicted.

major effect of a mountain on the advance of a density current is the retardation of the cold pool. When the depth of the density current is less than the mountain crest height or the static stability is large, the kinetic energy of the flow is too small to lift the air over the mountain and a complete upstream blocking of the density current can occur.

The current paper provides a natural extension to the studies of the smaller-scale topographically forced systems by Banta (1984, 1986), Wolyn and McKee (1994), and Bischoff-Gauss et al. (1989) to a regional scale. Furthermore, we examine in detail the MPS breakdown process in a real case study using both high-resolution 3D numerical simulations and mesoscale observations, whereas this process was only hypothesized by Tripoli and Cotton (1989a,b). Also, our study will for the first time examine another interesting important process—the generation of propagating mesoscale gravity waves—as the consequence of the westward-propagating density current first identified by Bossert and Cotton (1994a,b).

The gravity wave event to be investigated here occurred in Montana and the Dakotas region on 11–12 July 1981 during the Cooperative Convective Precipitation Experiment (CCOPE). Section 2 of this paper briefly reviews the pertinent aspects of the many observational and numerical studies of this gravity wave event that have already been published. The mesoscale model and the experiment design are documented in section 3. A comprehensive analysis of the control model results is conducted in section 4, and the results from the flat-terrain and adiabatic sensitivity tests are treated in section 5. A summary of the results and a conceptual model based upon this numerical investigation of this CCOPE event are presented in section 6.

2. Review of the CCOPE gravity wave event

The 11–12 July 1981 wave event has been previously analyzed with mesoscale surface and rawinsonde observations, radar and satellite imagery, multiple-Doppler radar wind analysis and pressure retrievals, and linear stability analysis (Koch and Golus 1988; Koch et al. 1988; Koch and Dorian 1988; Koch et al. 1993). Two episodes of gravity waves were identified passing the CCOPE network: from 1200 to 2000 UTC 11 July and from 0000 to 0800 UTC 12 July. Each episode consisted of a single packet of three to four waves. The first episode was characterized by bands of rainshowers, whereas the second one consisted of severe thunderstorm activity. In addition, each wave episode contained two gravity wave modes, characterized by dissimilar wavelengths and frequencies. The “wave-axis tracking method” applied to bandpass-filtered data determined that the primary mode had a wavelength of 150 km and phase speed of 15.2 m s^{-1} during the first wave episode, which is the time of relevance to the current study. The gravity waves in both wave episodes were discovered to have emanated from the general region of the Absaroka Mountains in extreme southwestern Montana.

Koch and Dorian (1988) hypothesized that geostrophic adjustment and shear instability were the two most likely wave source mechanisms during the second wave episode, but lack of data prohibited drawing any conclusions during the first episode. They were unable to assess the role of topography, nor any other mechanism operating on scales unresolved by the rawinsonde network. In addition, the earliest clear evidence of imbalance was not seen until 0000 UTC 12 July, yet the microbarograph analysis indicated that the first episode of gravity waves had already reached the CCOPE net-

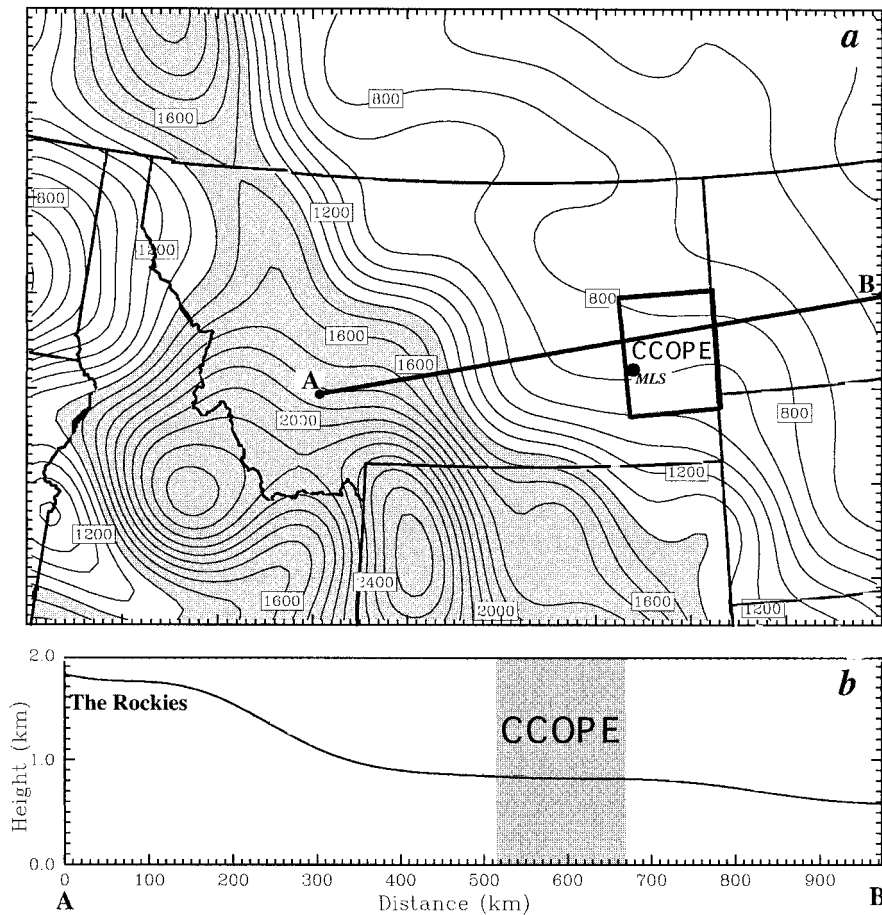


FIG. 3. Smoothed terrain data used in the MM5 simulation (contour interval 100 m). (a) Elevation higher than 1400 m is shaded to highlight the Rocky Mountain barrier. The thick line AB depicts the location of the cross sections used throughout the paper unless stated otherwise. Miles City is shown as MLS. (b) Cross section along AB of the terrain profile and location of the CCOPE mesonet.

work at least 12 h earlier. For example, surface pressure perturbation analyses over the CCOPE mesonet (Fig. 2) show that by 1500 UTC 11 July, wave crest R0 ($p' > 0$) and trough T0 ($p' < 0$) had already appeared over the mesonet [these analyses were obtained using the same procedures explained by Koch and Golus (1988)]. Therefore, it appears that another mechanism other than geostrophic adjustment associated with the upper-level jet was responsible for the generation of the first wave episode.

3. Model and experiments

The numerical model used in this study is the non-hydrostatic, primitive equation Pennsylvania State University–National Center for Atmospheric Research (PSU–NCAR) Mesoscale Model 5 (MM5) version 2. (Dudhia 1993; Grell et al. 1995). Our MM5 simulations were originally set up as a benchmark of the numerical investigation made of this case by Kaplan et al. (1997) using another model with a horizontal grid resolution

of 16 km. Our control experiment is a “fake dry” simulation, meaning that latent heating due to change of phase of water substances was suppressed throughout the model simulation. The Blackadar planetary boundary layer scheme and a radiative upper boundary condition were used. The model terrain and land use were interpolated from the 18.5-km-resolution NCAR archived data. The terrain is highly smoothed because it was subjected to 100 passes of a nine-point smoother (using $\gamma = 1/64$). Figure 3a shows the representation of the terrain in the model with elevations higher than 1400 m shaded. Line AB indicates the location of the vertical cross sections used throughout most of this paper, and the profile of the terrain along this cross section is depicted in Fig. 3b. The selected cross section is nearly perpendicular to the Absaroka Mountains in Montana, as well as being normal to the observed and simulated gravity wave fronts. The actual model domain size is about 10 times larger than that shown in Fig. 3a.

The model was initialized at 0000 UTC 11 July 1981 with National Meteorological Center (now operating as

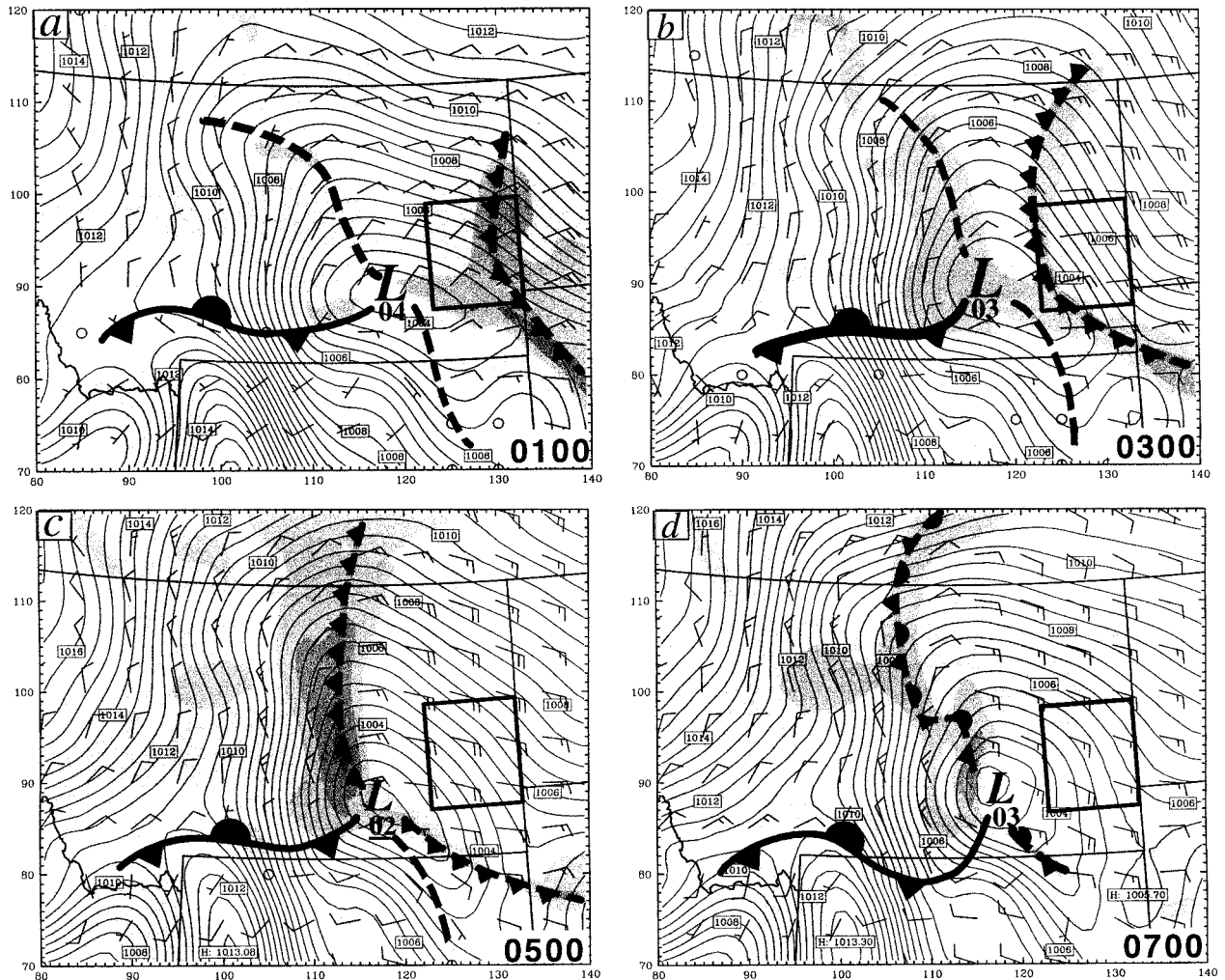


FIG. 4. Model forecast mean sea level pressure (contour interval 1 hPa), surface wind (full barb-5 m s⁻¹), and 850-hPa positive upward motion (shaded at interval of 3 cm s⁻¹) valid at (a) 0100, (b) 0300, (c) 0500, and (d) 0700 UTC 11 Jul 1981. Stationary fronts, lee troughs, and lee cyclone are all depicted in customary fashion, and the westward-propagating density current is depicted with small pips. CCOPE mesonet is shown by the rectangle.

the National Centers for Environmental Prediction) 2.5° grid data and then reanalyzed with conventional upper-air and surface observations. No mesonet data were used for reanalysis because of the extremely small size of the surface mesonet (Fig. 3a) and the few available CCOPE soundings. The observational reanalysis was also used to formulate the boundary condition in conjunction with a flow relaxation scheme. A 12-h spinup with *full microphysics* was attempted but failed because there was highly complex convective activity occurring during this period, and thus the model 12-h forecast of this spinup failed to compare well enough with observations. On the other hand, a 12-h spinup added to the fake-dry simulation did not produce an acceptable MPS, which naturally resulted in a poor simulation of the gravity wave.

To test the hypothesis to be developed from the above control simulation, results from two sensitivity tests also

will be discussed. One experiment uses the average height of 1500 m for the whole domain, that is, uniformly flat terrain, and the other is a totally adiabatic version of the control experiment. These experiments are designed to examine the influence of the topographic and diabatic processes on the generation and evolution of the density current and gravity waves.

4. Simulation results

a. Stage I: Westward propagation of remnant MPS in the form of a density current

We begin by examining the control run forecasts of the mean sea level pressure field from 0100 to 0700 UTC 11 July 1981. Just before sunset (0100 UTC), the surface wind fields (Fig. 4a) display a continuous leeside convergence from central Montana to northeastern Wy-

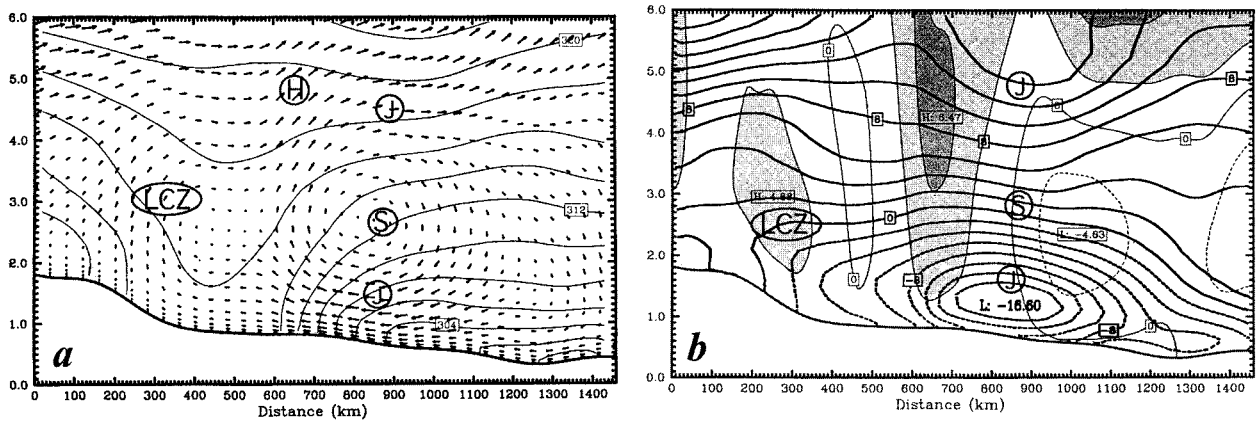


FIG. 5. Vertical cross section from control run forecast for 0100 UTC 11 Jul 1981: (a) potential temperature ($\Delta = 2$ K) and vertical circulation in the cross-section plane, and (b) horizontal wind in the plane of the cross section (thick lines, positive values represent winds directed from left to right, $\Delta = 2$ m s^{-1}) and vertical motion (thin lines, $\Delta = 3$ cm s^{-1}) with upward motion shaded. Cross-section location has the same starting point as "A" in Fig. 3a, but extends farther east to the border of North Dakota and Minnesota. LCZ denotes the location of the leeside convergence zone, H is the relative high pressure, Js are the inflow and outflow jets, and S is the center of the MPS circulation.

oming in the warm lee trough. This is the area where the gravity wave will be generated later. Another convergence zone with relatively strong upward motion in extreme eastern Montana at 0100 UTC propagates westward and merges with the leeside convergence zone by 0500 UTC. This propagating feature is shown below to be the remnant of the daytime MPS. A subsynoptic lee cyclone immediately to the west of the CCOPE mesonet in southern Montana is embedded in the lee trough. A stationary front that will be referred to as the "orographic front" extends from the lee cyclone along the Montana–Wyoming border. This front was also evident in the potential temperature fields (not shown). To the east of the lee trough, surface winds are upslope with even stronger easterly wind to the east of the MPS convergence boundary. To the west of the lee trough and north of the orographic front, surface winds are northerly while to the south of this front winds are primarily westerly. During this 6-h period, both the orographic front and the lee cyclone are quasi-stationary features.

Vertical cross sections cut through both convergence zones in eastern Montana (Fig. 5) reveal that the initial fields of the simulation are to a large extent consistent with phase 3 of the conceptual MPS model of Wolyn and McKee (1994), as depicted in Fig. 1d. The cross sections in Fig. 5 lie along the same path as shown in Fig. 3 but extend 500 km farther east to show the broad MPS circulation. Notice in particular the ascent within the leeside convergence zone located at the foot of the mountains, the migrating solenoid, the westerly and easterly wind maxima above and below the solenoid center, and the lee trough (at $x = 450$ km).

Although the fields shown in Fig. 5 are obtained from just a 1-h forecast from the model, the important features just discussed all display continuity and a gradual evolution over the next several hours of simulation time,

as demonstrated in Fig. 6. Notice that the lee trough remains nearly stationary or retrogrades slightly, whereas the solenoid center retreats rapidly westward at a speed of 18.5 m s^{-1} . The horizontal potential temperature gradient across the easternmost convergence zone (i.e., the one associated with the solenoid) is nearly 8 K $(100$ km) $^{-1}$. A pronounced cold pool is located to the east of this convergence line in North Dakota and extending eastward to the Great Lakes (Fig. 5a). The stability at the top of the cold pool has been strengthened by the sinking branch of the daytime MPS.

The leeside convergence zone and its associated updraft (U1) may seem to gradually fade away by 0400 UTC, but this is not actually the case. Rather, this updraft becomes indistinguishable from that produced by the solenoid convergence zone (U2) as the latter feature propagates westward and merges with the leeside convergence zone. Prior to their merger, these convergence zones surrounded the subsynoptic lee cyclone in southeastern Montana.

As strong near-surface easterly flow on the northern side of the lee cyclone continuously advects cooler, denser air from the cold pool region westward over eastern Montana, the density differences across the solenoidal convergence zone are strengthened. The thermal advection creates an even stronger horizontal pressure gradient force in the plane of the cross section ($-\rho^{-1}\partial P/\partial x$) than before (Fig. 7a). This analysis indicates that the upslope flow was largely driven by this horizontal force, since the strongest easterly wind is collocated with the greatest negative pressure gradient force and the greatest deceleration occurs where this force vector switches direction (at $x = 450$ km at 0200 UTC). Over the course of the next 3 h, very strong localized convergence and an updraft jet are created as the solenoid and the associated cold pool advance westward to the foot of the mountains. This migration, in

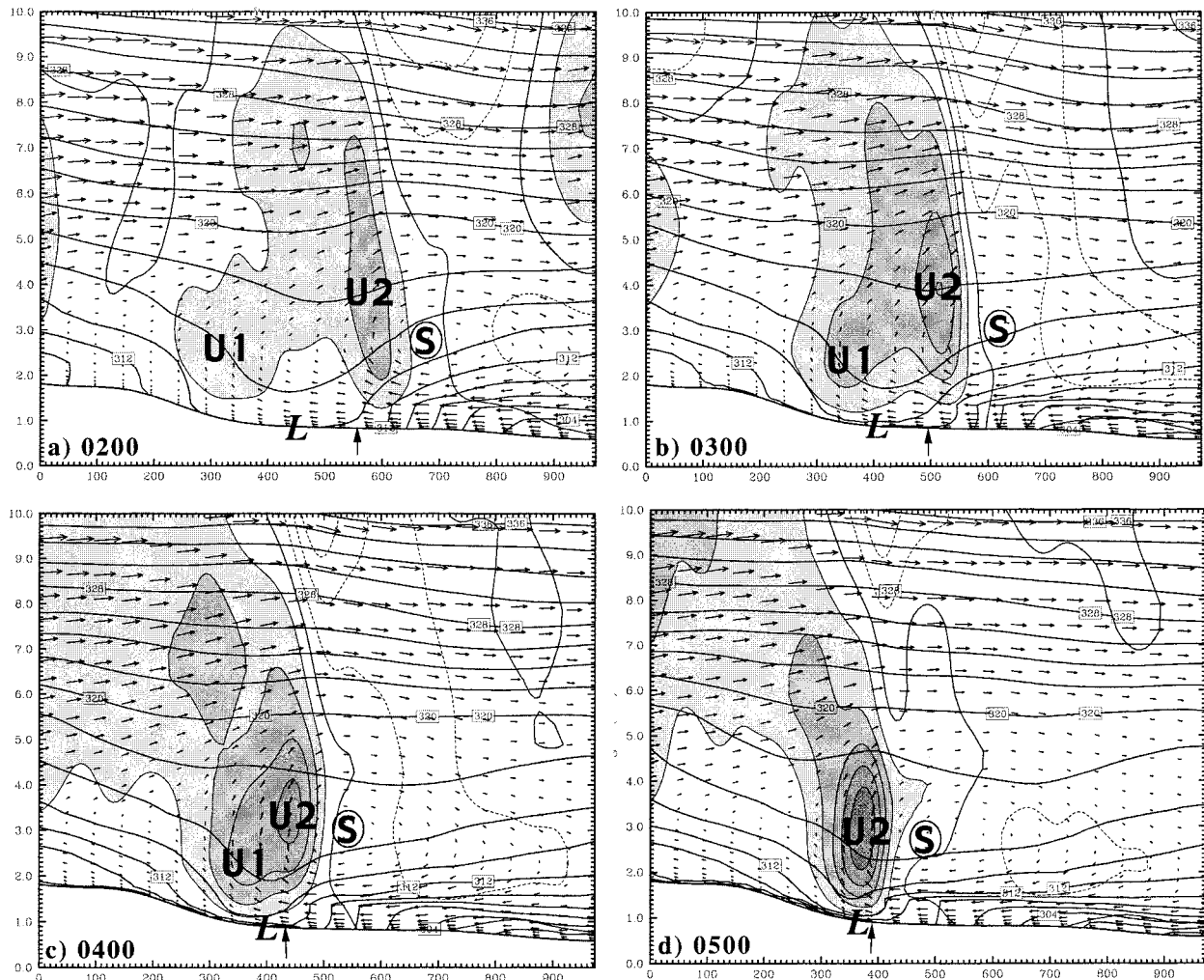


FIG. 6. Cross sections of forecast potential temperature (solid lines, $\Delta = 2$ K), vertical velocity ($\Delta = 3$ cm s $^{-1}$ with shaded area $w > 3$ cm s $^{-1}$), and vertical circulation from the control circulation at (a) 0200, (b) 0300, (c) 0400, and (d) 0500 UTC 11 Jul 1981. The arrow indicates position of the density current front, L denotes the center of the lee cyclone, S shows the solenoid center, U1 and U2 are the two updraft centers discussed in the text.

conjunction with a very pronounced opposing pressure gradient, effectively strengthens the remnant leeside convergence zone (Fig. 7b).

The strong cold advection over the plains causes the air in eastern Montana and the Dakotas to cool much faster than the low-level atmosphere over the lee slope of the mountains. Surface observations showed that temperature decreased by only 3°C from 0200 to 0800 UTC at Lewistown (LWT), the only synoptic station located in the steep eastern slope of the Rockies in Montana. Cooling at Miles City (MLS) and Jordan (JDN), which are located on the plains in eastern Montana, was as much as 8°C.

This westward-propagating up-branch of the remnant daytime MPS is similar in character to the observational and numerical study of thermally driven flow across the Colorado mountain barrier by Bossert and Cotton

(1994a,b). They identified four distinct phases of the MPS over a complete diurnal cycle in their conceptual model of the evolution of the regional-scale MPS circulation. In phase I, a deep MPS develops from heating of the eastern slope of the Front Range during the daytime (Fig. 8a). The MPS has a low-level upslope branch, a vertical branch, and an outflow or return branch (at 5–6 km above ground level). During phase II (the late afternoon), this circulation transforms into a WPDC as the elevated terrain heating diminishes (Fig. 8b). In the third (nocturnal outflow) phase, the WPDC moves westward across the mountains (Fig. 8c). Their model simulation suggested that the WPDC circulation is widespread over the entire north–south extent of the eastern slope of the Colorado Front Range.

During the third phase, which lasts for roughly 3 h after sunset (0200–0500 UTC in the present case), the

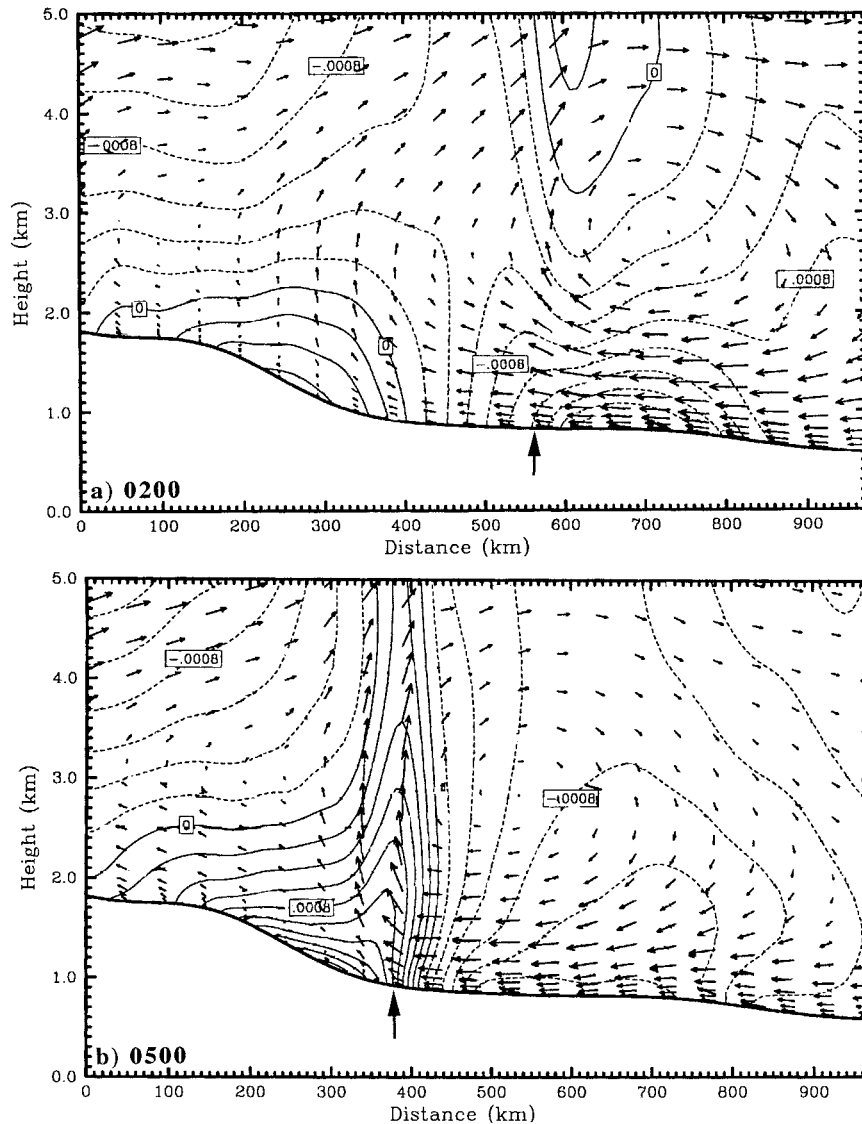


FIG. 7. Cross sections of simulated horizontal pressure gradient force ($\Delta = 0.0002 \text{ m s}^{-2}$) (dashed and solid light lines represent leftward- and rightward-directed forces) and vertical circulations at (a) 0200 and (b) 0500 UTC 11 Jul 1981. The arrow indicates position of the density current front.

WPDC was identified as a density current by Bossert and Cotton (1994a,b) by use of the densimetric formula for a steadily propagating density current:

$$c = k \left[gh \left(\frac{\Delta\theta}{\theta_0} \right) \right]^{1/2}, \quad (1)$$

where c is the propagation speed of the density current, k is an empirically determined Froude number, g is gravity, h is the depth of the current (generally taken as the mean height of the advective flow far behind the current head), $\Delta\theta$ is the potential temperature difference associated with the density current, and θ_0 is the mean potential temperature. Assuming $k = 1$, they estimated a density current speed of $6.5\text{--}7.8 \text{ m s}^{-1}$, which com-

pared favorably to the simulated propagation speed in their simulation of $5\text{--}7 \text{ m s}^{-1}$.

In our case, the head of the cold pool propagates westward by 180 km over the 3-h period beginning at 0200 UTC, giving an average speed of 16.7 m s^{-1} . For a temperature contrast of $\Delta\theta = 8 \text{ K}$ (Fig. 6), $\theta_0 = 310 \text{ K}$, $h = 900 \text{ m}$, and $k = 1$, the estimated speed is 15.1 m s^{-1} . Simpson and Britter (1980) argue that the effects of a tailwind must be accounted for ($0.62U$). If it can be assumed that the "ambient" wind occurs directly upwind of the cool pool core (i.e., $U = 4 \text{ m s}^{-1}$ at $x = 1450 \text{ km}$ in Fig. 5b), then the final estimate for the speed of the density current is 17.6 m s^{-1} . This result and the previous discussion of the pressure gradient force sug-

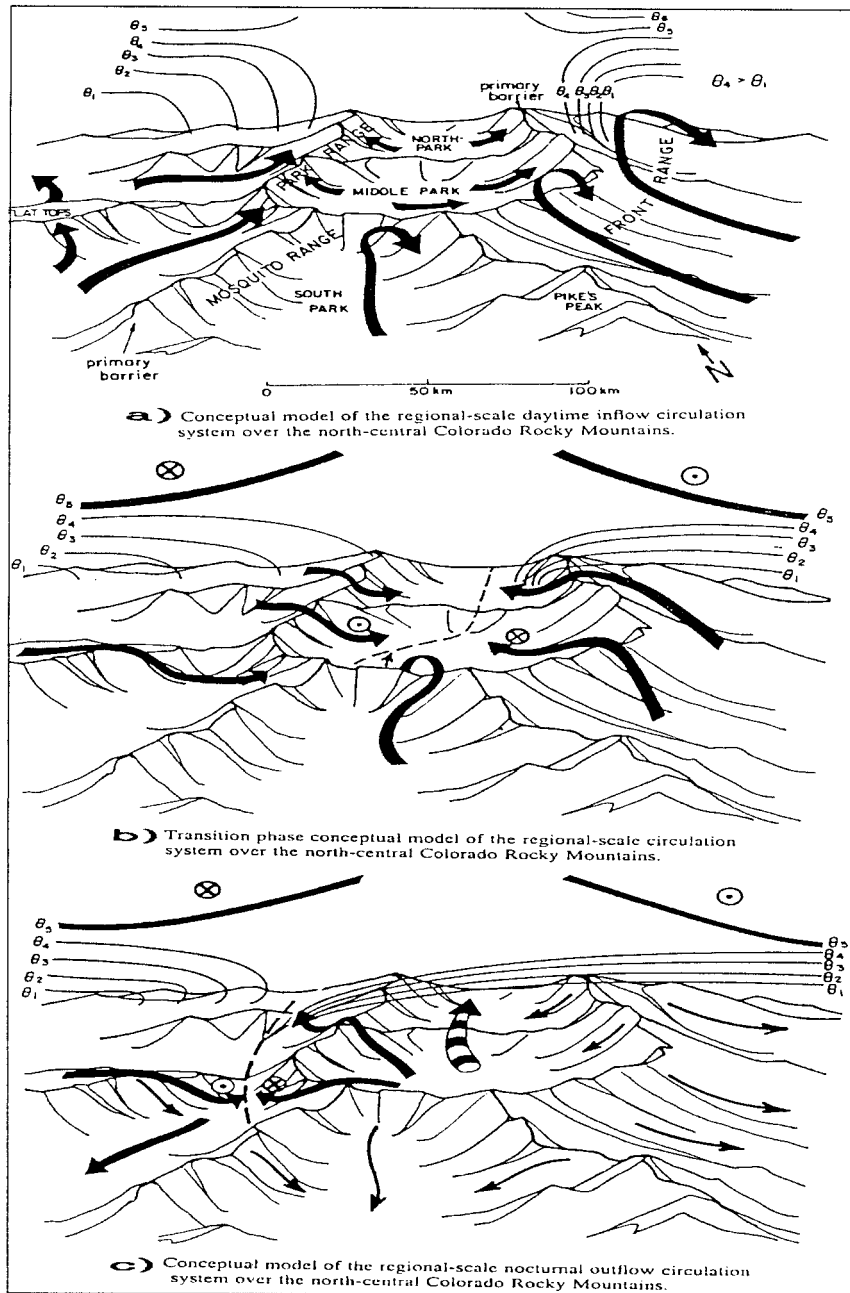


FIG. 8. Conceptual model of 24-h evolution of terrain-induced circulation over the north-central Colorado Rocky Mountains: (a) daytime inflow circulation, (b) transitional phase, and (c) nocturnal outflow circulation. The arrows show the relative airflow, the dashed line denotes the location of the density current, the thin solid lines are isentropes, and the cross and dot points, respectively, denote southerly and northerly jets (after Bossert and Cotton 1994a).

gest that this cold pool may have the nature of a propagating density current; however, additional evidence is needed.

According to Simpson (1987), Smith and Reeder (1988), and Koch et al. (1991), a suspected density current must also exhibit a region of positive front-relative “feeder” flow behind the leading edge of the density

current. Front-relative flow at 0200 UTC obtained by subtracting the mean propagation speed of the density current (16.7 m s^{-1}) from the front-normal winds is shown in Fig. 9a. A pronounced feeder flow does indeed exist behind the leading edge of the density current with a maximum of $3\text{--}4 \text{ m s}^{-1}$. The feeder flow has the same strength at 0300 and 0400 UTC, but it has nearly dis-

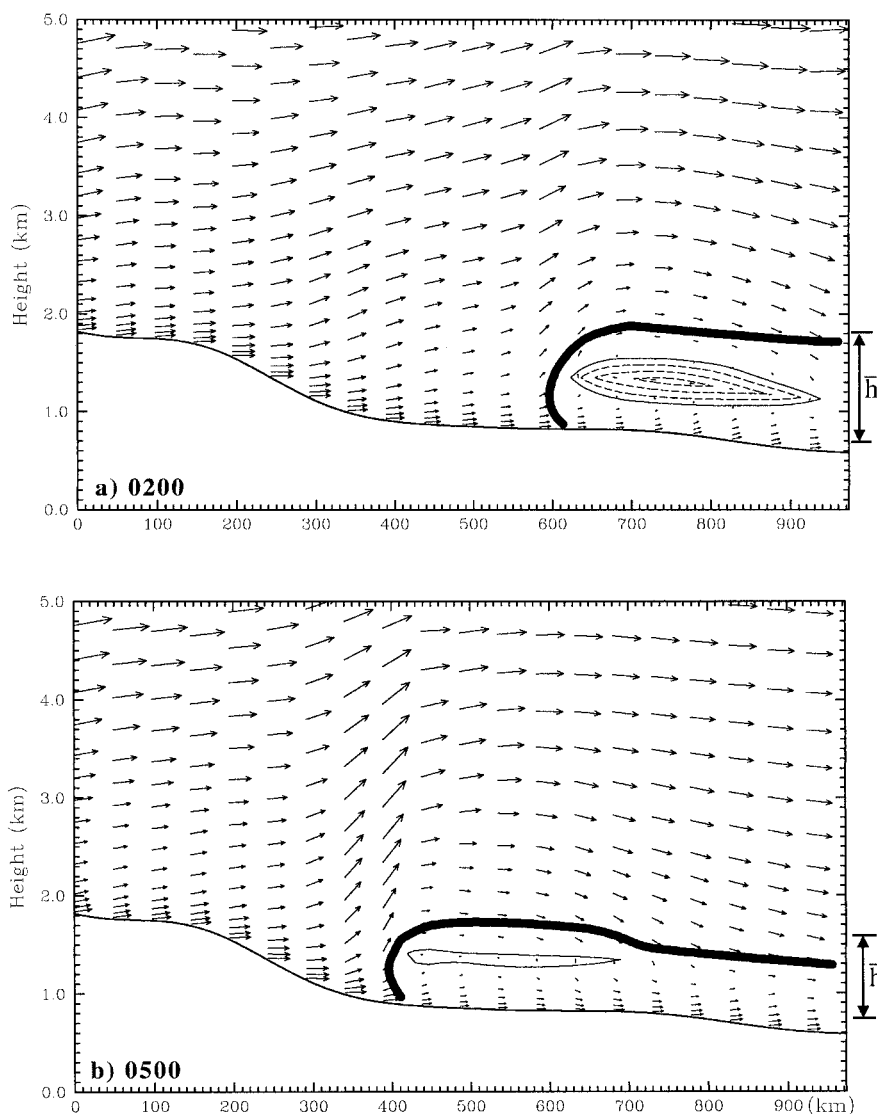


FIG. 9. Flow relative to the density current from the control simulation for (a) 0200 and (b) 0500 UTC. Dashed lines indicate the “feeder flow” region of the westward-propagating density current ($U - C < 0$ ($\Delta = 0.5 \text{ m s}^{-1}$)). The thick solid line denotes the average depth of the density current (h).

appeared by 0500 UTC (Fig. 9b). The reason for this happening is that the cross-front pressure-gradient force that drives the density current westwards has greatly diminished as the current depth and density contrast have weakened.

The depth of the hypothesized density current also should be found to be in good agreement with that predicted hydrostatically from the surface temperature and pressure difference between the cold and warm region according to

$$h = \frac{T_c(p_c - p_w)}{\rho_w g[(p_c/p_w)T_w - T_c]} \quad (2)$$

The subscripts c and w indicate variables, respectively,

in cold and warm air. Although the application of (2) is very sensitive to the assumptions made (Smith and Reeder 1988), a crude estimate can be made as follows. Since the mean sea level pressure difference across the 200-km transitional zone of 8-K temperature difference at 0200–0300 UTC (Fig. 6) is 2.5 hPa, then we estimate $h \cong 1.0 \text{ km}$. This value is in excellent agreement with the model depth (0.9 km).

For all the above reasons, we conclude that the WPDC has the characteristics of a density current. Observational evidence for the simulated WPDC can best be seen in the detailed mesonet observations, though only in a rather small area. Surface mesoanalysis of the wind vectors and isentropes at 0100 and 0200 UTC 11

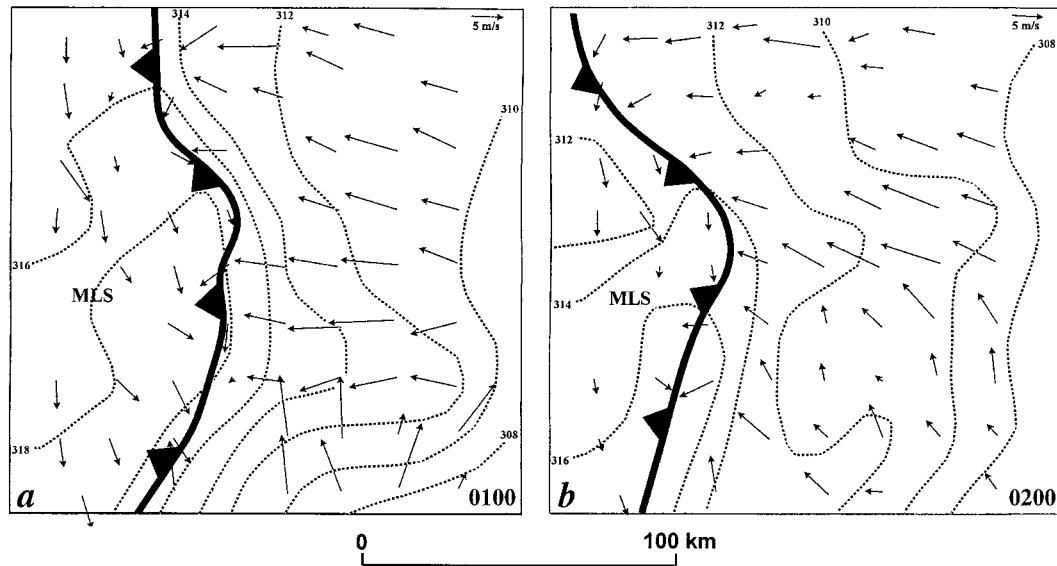


FIG. 10. Observational evidence for the westward-propagating density current. Shown displayed are wind vectors at the mesonet stations and subjectively analyzed potential temperature ($\Delta = 2$ K) over the CCOPE surface mesonet network (cf. Fig. 3) at (a) 0100 and (b) 0200 UTC 11 Jul 1981. The frontal feature indicates location of the leading edge of the density current front.

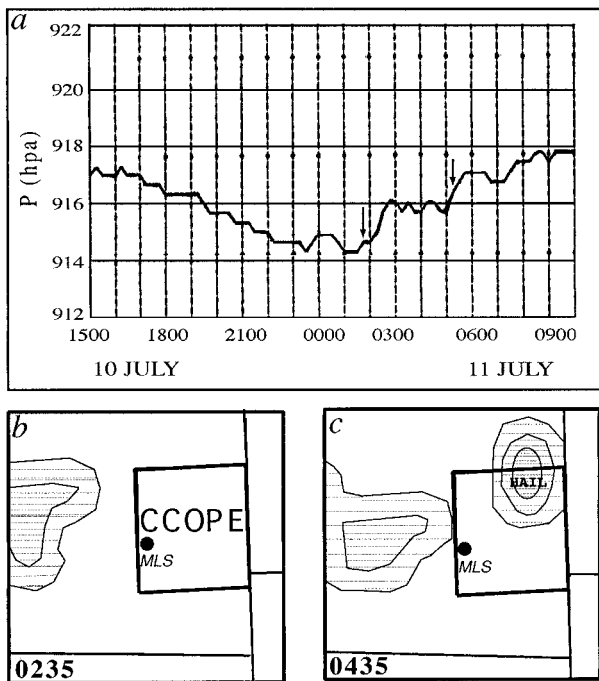


FIG. 11. (a) Microbarogram record (hPa) from MLS (Fig. 3) from 1500 UTC 10 Jul to 1000 UTC 11 Jul 1981. Two major pressure pulse events are marked with arrows: the first corresponds to the westward-propagating density current and the second is related to nearby thunderstorm activity. (b) and (c) The radar summaries, respectively, at 0235 and 0435 UTC near the CCOPE mesonet network. Echo intensities shown correspond to 30, 41, and 46 dBZ.

July 1981 (Fig. 10) reveals a marked convergence boundary separating air that is approximately $6^{\circ}\text{--}8^{\circ}\text{C}$ cooler from air to the west. The location of this westward-propagating convergence boundary is in general agreement with the simulated density current shown in Fig. 4. Microbarograph data from Miles City (Fig. 11a) also shows an apparent pressure jump of 1.5 hPa at approximately 0215 UTC during the passage of this convergence boundary, with a second pressure jump of 1.0 hPa at 0500 UTC. The second pressure jump may be due to cold outflow from nearby thunderstorms (Fig. 11c); note that there are no thunderstorms near Miles City during the occurrence of the first pressure jump (Fig. 11b). Although the average propagation speed of the density current in the surface observations over the CCOPE area is only 8.5 m s^{-1} ($\sim 50\%$ of that simulated), this speed is consistent with the observed 1.5-hPa pressure jump according to (1), assuming a correspondingly shallower current as per (2).

What causes this density current? Development of the shallow westward-propagating density current occurs in the early evening when the diminishing surface heating can no longer sustain the baroclinicity of the daytime MPS. Since there is a strong density difference across the two sides of the remnant daytime MPS, this thermally induced convergence zone can be advected back toward the mountain. Thus, the formation of the density current may be described as the reversal of the daytime MPS. Topographic asymmetry and especially the difference of the elevation between terrain and plains are essential to the formation of the WPDC, as explained by Bossert and Cotton (1994a,b). The large difference between the propagation speed in our simulation and

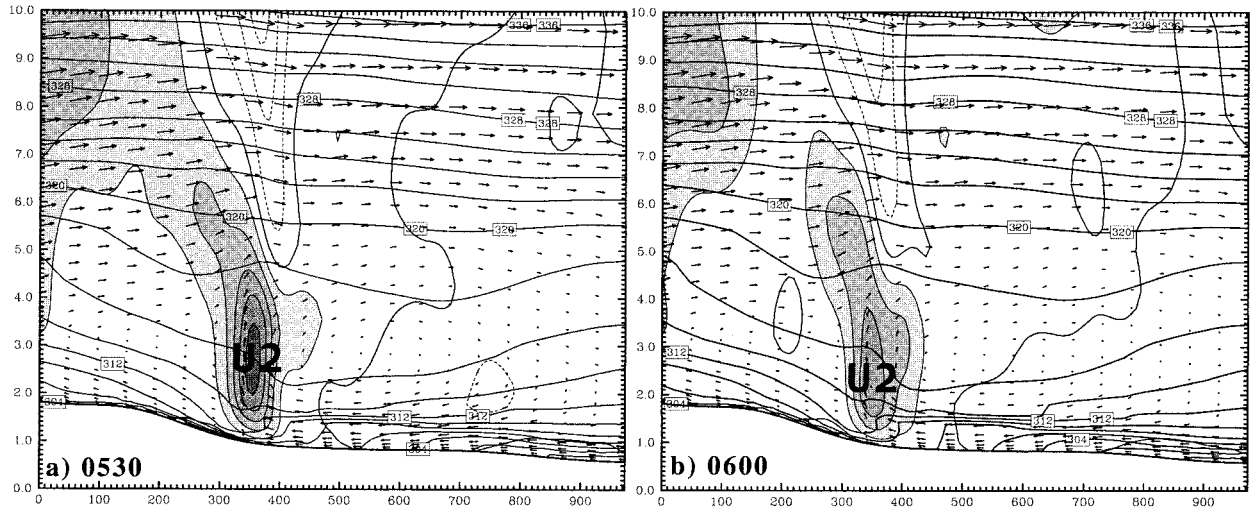


FIG. 12. As in Fig. 6 except for (a) 0530 and (b) 0600 UTC.

that by Bossert and Cotton (1994a) is likely due to the relatively greater mountain heights and steeper terrain slope in the current case. Since the mountain height in the CCOPE simulation is nearly twice that in their simulation, a relatively stronger cold pool can develop in our model simulation. However, as we will see next, a stronger cold pool does not guarantee that it will be able to make it across the mountain crest.

b. Stage II: Orographic blocking of density current and mesoscale isentropic ridge development

From slightly before 0530 to 0600 UTC, the westward-propagating density current decelerates to a complete rest as it becomes blocked at the foot of the steepest terrain (Fig. 12) and merges with the original leeside convergence zone (Fig. 4c). The blocking results in even stronger upward motion (compared to the original updraft U1) and a more focused convergence zone. This turns out to be a transitional stage lasting for a little more than 1 h, during which near-surface cold air from the former cold pool is advected into the original warm trough, where it rapidly decelerates.

A mesoscale isentropic ridge begins to appear aloft coincidentally with the occurrence of blocking, particularly in the lower levels (e.g., $\theta = 316$ K). The relative contributions to the local change of the potential temperature can be evaluated through the thermodynamic equation applicable to a two-dimensional atmosphere (no y variations):

$$\frac{\partial \theta}{\partial t} = -u \frac{\partial \theta}{\partial x} - \frac{\theta_0}{g} N^2 w + \dot{\theta}. \quad (3)$$

The three terms on the right-hand side of (3) are, respectively, the horizontal temperature advection, the adiabatic effect due to vertical motion, and the diabatic effect. The first two terms are evaluated in terms of their

separate (Figs. 13c and 13d) and combined (Fig. 13b) effects on the hourly potential temperature difference between 0500 and 0600 UTC. Adiabatic cooling is the dominant factor in the buildup of the mesoscale isentropic ridge in the middle to lower troposphere, whereas the horizontal temperature advection is greatest near the ground (inside the inversion layer). The combined (adiabatic) effects of the horizontal and vertical temperature advection (Fig. 13b) are responsible for essentially all of the temperature change (Fig. 13a) during this hour. This serves as the justification for neglecting diabatic effects in this analysis of this fake-dry (though diabatic) simulation. Banta (1984) also pointed out the adiabatic cooling effect caused by the upslope wind associated with a mountain–valley circulation. Also note the adiabatic warming resulting from the subsiding branch of the MPS circulation and how it maintains the strong stability atop the cool pool, as asserted earlier.

There are two reasons why the westward-propagating density current was blocked at the foothills, rather than “spilling over” the other side of the mountains as in the simulation performed by Bossert and Cotton (1994a). First, the Froude number is estimated as $F = U/NH = 0.86$ (from the phase speed of the density current $U = 16.7 \text{ m s}^{-1}$, the height of the mountain relative to the plains $H \sim 1.5 \text{ km}$, and the mean Brunt–Väisälä frequency $N = 0.013 \text{ s}^{-1}$). This indicates that the density current did not have enough kinetic energy to climb up and over the mountain. Since the mountain was much lower in the simulation of Bossert and Cotton (1994a), the density current could pass across the mountain and their flow was able to evolve to the nocturnal phase IV. Second, nocturnal cooling has created an extremely shallow layer of cold, highly stratified air over the lee slopes by 0500 UTC (Fig. 6). Since the near-surface air over the lee slope has already been made much denser than the nearby “free atmosphere” at the

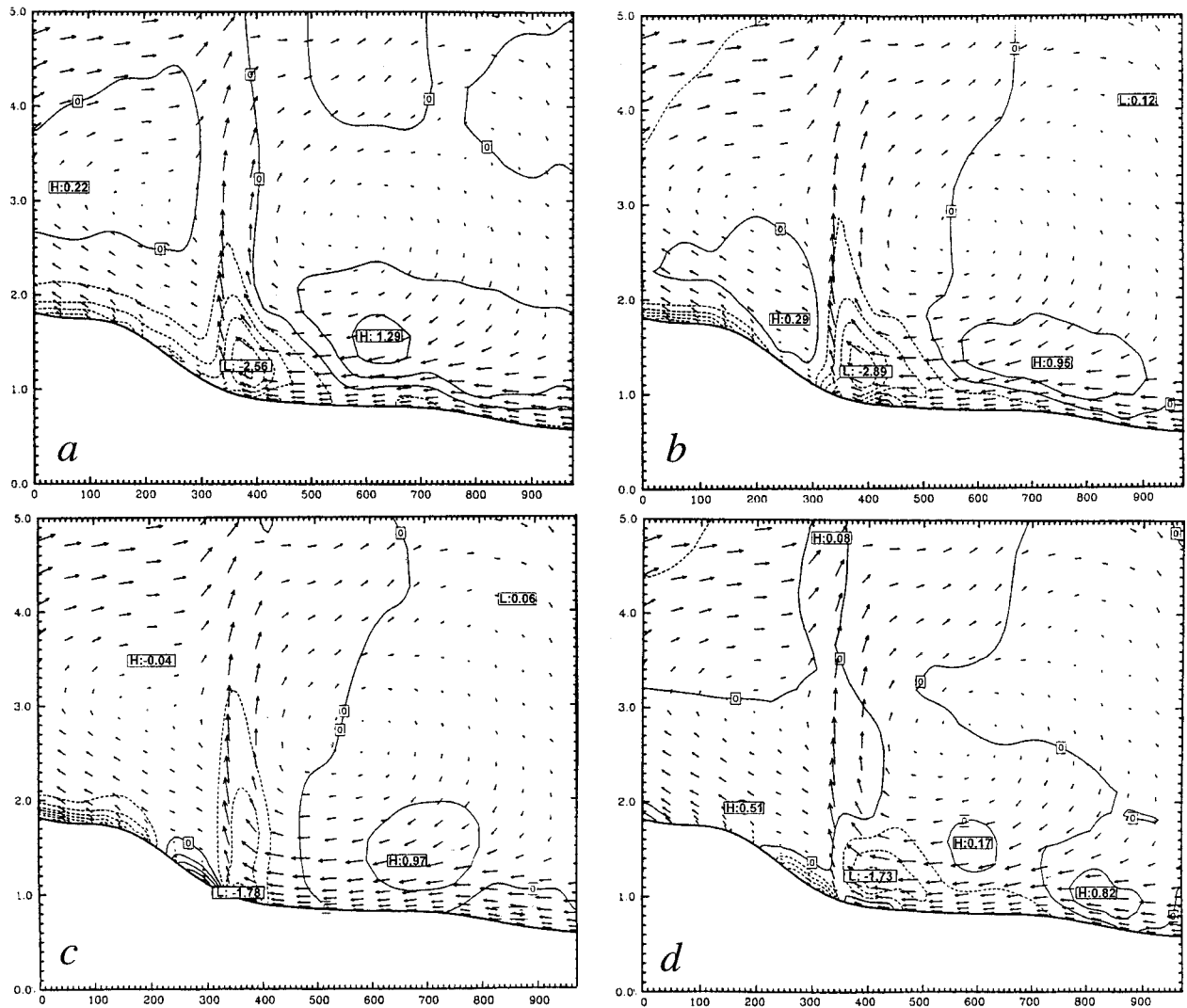


FIG. 13. Control run forecast of (a) temperature change between 0500 and 0600 UTC 11 Jul 1981, (b) mean hourly temperature change due to both horizontal and vertical temperature advection, (c) mean temperature change due only to vertical temperature advection (adiabatic cooling), and (d) mean temperature change due only to horizontal temperature advection over the same time period ($\Delta = 0.5$ K; dotted lines indicate cooling and the arrows show vertical circulation at 0600 UTC).

same altitude, a shallow but strong eastward-directed pressure gradient force is created opposing the developing MPS (Fig. 7b). This opposing force finally strengthens to the point where it effectively blocks the WPDC from advancing farther westward. Consequently, strong, quasi-stationary convergence develops just to the east of the steepest slope of the Rocky Mountains.

The strongest upward motion is reached at ~ 0530 UTC (Fig. 12a) and weakens gradually afterward. Weakening of this updraft occurs because, as the isentropic ridge develops, it begins to generate a separate upward motion center to its east (U3) in response to the strengthening eastward horizontal pressure gradient force in the 2–4-km layer (Fig. 14). This developing isentropic ridge and the new updraft are the embryo of the gravity wave that will soon appear.

c. Stage III: Isentropic ridge develops into gravity wave

At the end of the transition period (0624 UTC), the newly generated upward motion center to the east of the isentropic ridge becomes for the first time stronger than the former updraft associated with the density current (Fig. 14b). The formerly singular updraft splits into two centers, one at midlevels (U3) and the other near the surface (U2). The low-level updraft center is associated with the weakening density current and disappears altogether by 0648 UTC (Fig. 14d), at which time a subsidence center begins to develop to the west of the isentropic ridge. A mesoscale gravity wave finally develops by 0700 UTC with the characteristic quadrature phase between the isentropic surfaces and the ver-

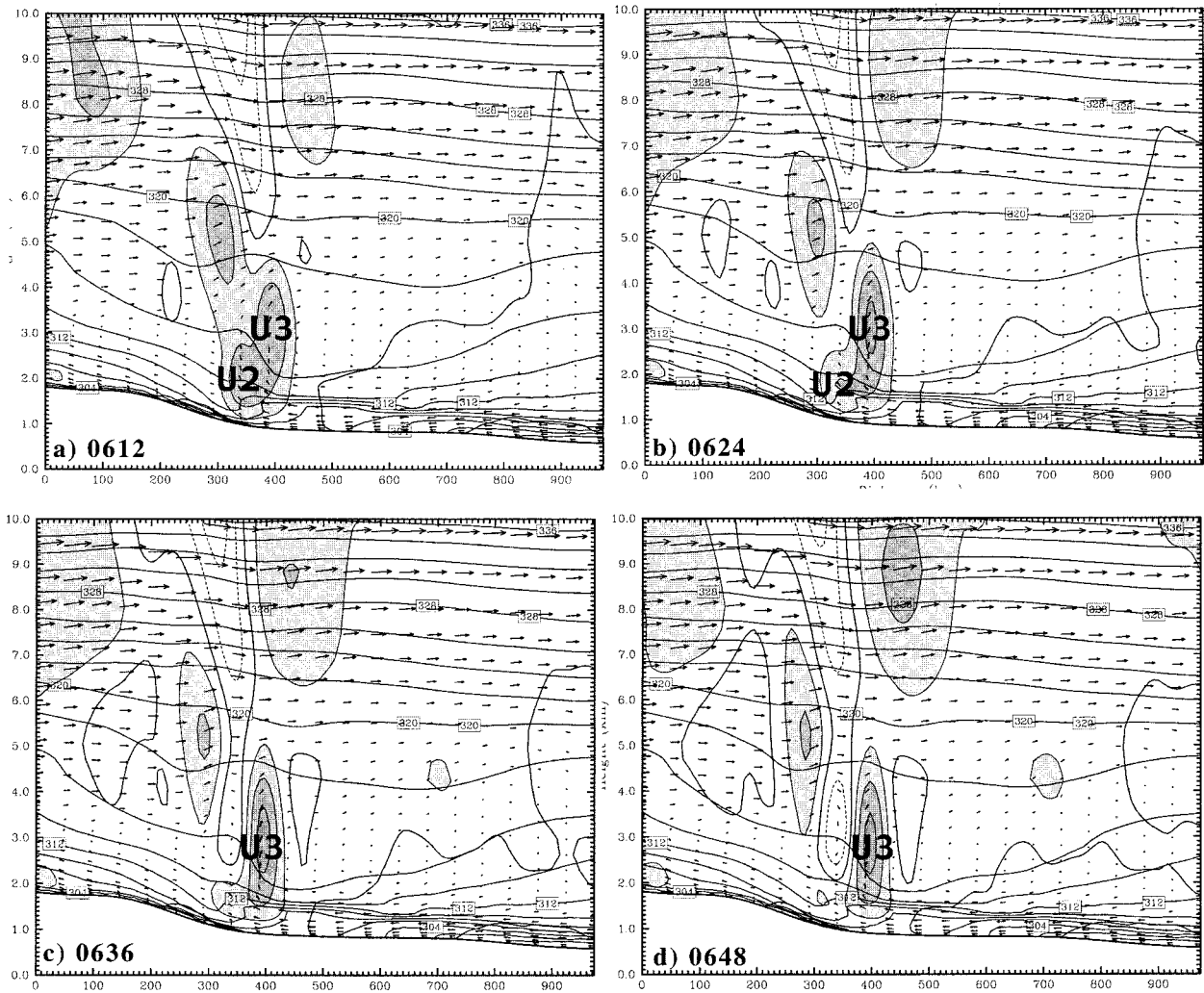


FIG. 14. As in Fig. 6 except for (a) 0612, (b) 0624, (c) 0636, and (d) 0648 UTC 11 Jul 1981.

tical motions. The distance between the upward and downward motion centers is 75 km. The 150-km wavelength of this newly generated gravity wave in the model exactly equals that observed by Koch and Golus (1988).

d. Stage IV: Mesoscale gravity wave propagates eastward in a well-defined duct

Although the gravity wave is vaguely seen in the simulated mean sea level pressure field at 0800 UTC (not shown), it becomes quite apparent by 0900 UTC. The wave propagates eastward with the subsynoptic low (this is the first time that the lee cyclone becomes progressive) and arrives at the CCOPE network by 1100 UTC (Figs. 15a,b and 18b). The first gravity waves composing observed wave episode I also first appeared between 1100 and 1200 UTC according to Koch et al. (1988).

Comparisons are first drawn between the model surface fields and soundings and the available CCOPE spe-

cial observations in order to have an appreciation of how well the model reproduced the observed thermal and wind fields relevant to ducting, before we investigate the ducting properties in detail. First of all, we find that the 12-h synoptic-scale surface forecast of pressure and winds (Fig. 15b) compares well to the observational analysis (Fig. 15c). The ability to draw comparisons with soundings is hampered by the fact that the special CCOPE soundings were not made until after 1900 UTC, which is several hours beyond the time frame of this study. The only sounding near the CCOPE mesonet network was that at Glasgow (GGW). Comparison of the observed and simulated soundings at GGW valid at 1200 UTC (Fig. 16) reveals that the model captures well the thermal structure of the atmosphere. However, the model is more moist than observed (the fake-dry run allows the atmosphere to become saturated without impacting the thermodynamic equation), and winds in the low to midtroposphere are too southerly.

Direct comparison between the simulated gravity

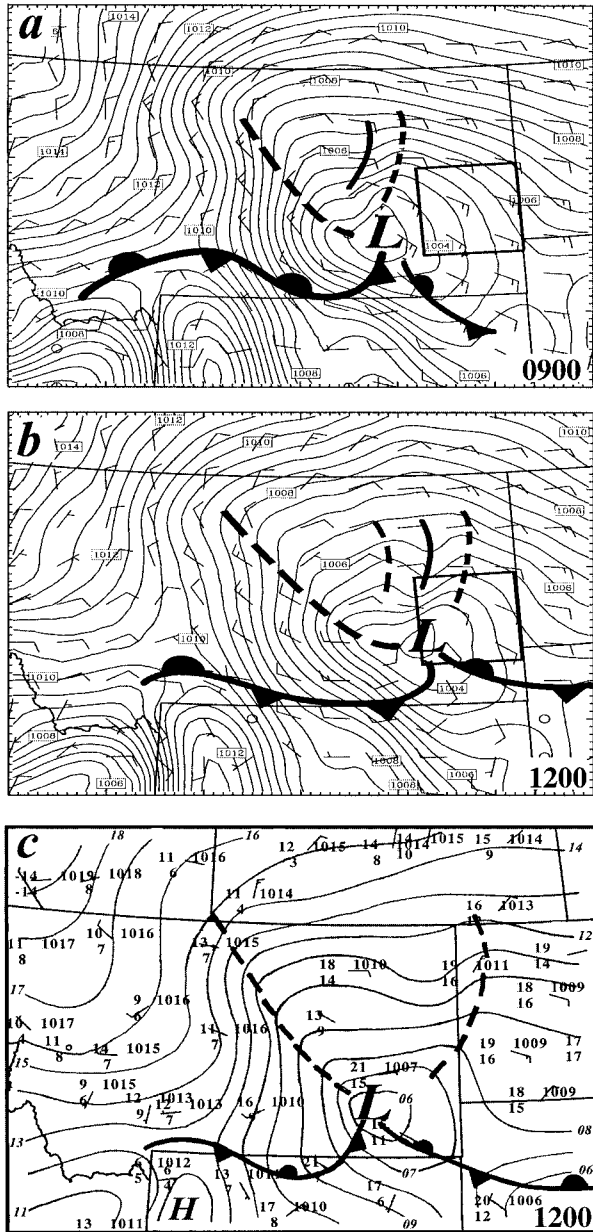


FIG. 15. (a) and (b) As in Fig. 4 except for (a) 0900 and (b) 1200 11 Jul 1981; (c) subjective surface observational analysis at 1200 11 Jul 1981. The dashed lines depict gravity wave troughs.

waves and those observed is facilitated by examining the mean sea level pressure fields forecast by the model directly over the CCOPE mesonet network (Fig. 17), and the bandpass-filtered surface pressure fields from the mesonet observations (Fig. 2). Notice first of all that the low-level upward motions precede the wave crest by one-quarter of a wavelength, as is expected for a propagating mesoscale gravity wave. The original singular wave later evolved into a train of two to three propagating waves (Fig. 15b). Each of these waves has the right pressure–wind phase relationship for mesoscale

gravity waves and has similar characteristics to the leading wave. The average phase speed of the gravity wave throughout the simulation is $\sim 10.2 \text{ m s}^{-1}$, though it is 11.5 m s^{-1} over the CCOPE mesonet network. On the other hand, the observed wave speed over the mesonet network is 15.2 m s^{-1} . This 24% phase speed discrepancy is largely due to the model error in the forecast winds around the overreflection level near 5 km, as discussed above (Fig. 16).

With the noted differences discussed above, there is ample justification to use the model forecasts to examine the wave maintenance mechanisms in detail. Wave overreflection and wave ducting can both explain why the simulated gravity waves persisted for such a long period of time. Jones (1968) showed that there is a critical value of the Richardson number ($\text{Ri} = 0.115$), below which the reflected wave has a larger amplitude than the upwardly propagating incident wave (it is “overreflected”). In fact, the average Richardson number in the shear layer surrounding the critical level is $\text{Ri} \sim 0.01$ (Fig. 18a). Wave overreflection was analyzed in the present case using Model II of Jones (1968), in which a shear layer is bounded below and above by layers of constant speed. For the simulated wavelength of 150 km, phase speed $C = 10.2 \text{ m s}^{-1}$, and mean Brunt–Väisälä frequency $N = 6 \times 10^{-3} \text{ s}^{-1}$ (Fig. 18a), the corresponding wave frequency $\omega = kC = 4.3 \times 10^{-4} \text{ s}^{-1}$ and $\beta = N^2/g = 4 \times 10^{-6} \text{ m}^{-1}$. Hence, we find values for his nondimensional parameters for frequency $\Omega = \omega/N = 4.3 \times 10^{-2} \text{ s}^{-1}$ and horizontal scale $j = \beta/(4k^2 + \beta^2)^{1/2} = 0.04$, from which we conclude that the requirements for overreflection are fully satisfied in our case. Therefore, the simulated average wave phase speed is approximately the wind speed at this overreflection layer.

Wave ducting of mesoscale gravity waves proposed by Lindzen and Tung (1976) was also examined. A combination of nocturnal radiative cooling and the passage of the cold air within the density current built up a 1.3-km-thick stable layer with mean $N = 0.012 \text{ s}^{-1}$ in the low levels before the gravity wave arrived. This duct layer is overlain by a layer containing small static stability from 3 to 6 km (Fig. 18a). The stable layer is roughly one-quarter of the vertical wavelength. A single critical level (thick dashed line) exists in the less stable layer and the Richardson number is sufficiently small ($\text{Ri} < 0.25$) in a small region surrounding the critical level and directly above the incipient gravity wave (Fig. 14a). This environment provides an excellent wave duct. The intrinsic ducted wave speed is given as

$$C_{d,n} = \frac{ND}{(\pi/2 + n)}, \quad (4)$$

where n indicates different vertical wave modes and N includes the liquid water effect. For the primary mode ($n = 0$), and assuming within the duct layer of depth $D = 1.3 \text{ km}$ that $N = 0.012 \text{ s}^{-1}$, the predicted ducted

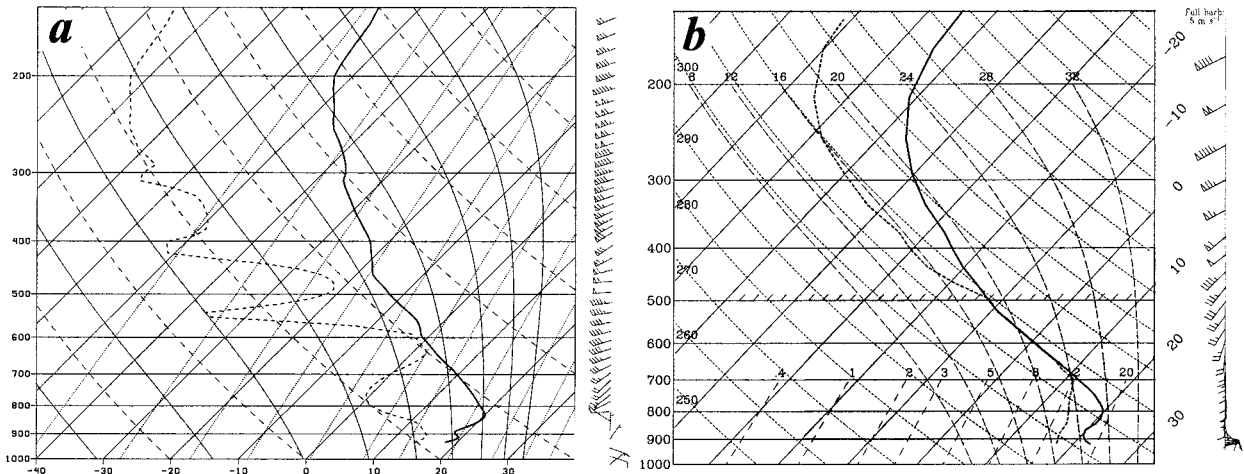


FIG. 16. Sounding in skew T -log p format for Glasgow (GGW), Montana, for 1200 UTC 11 Jul 1981: (a) observation and (b) MM5 12-h forecast.

wave speed $C_d = 9.9 \text{ m s}^{-1}$, which compares well to the average simulated phase speed of 10.2 m s^{-1} .

In summary, the necessary conditions for both wave ducting according to (Lindzen and Tung 1976) and for overreflection (Jones 1968) are satisfied for the simulated gravity waves. We conclude it is for this reason that the gravity waves generated by the isentropic perturbation prior to 0700 UTC (Fig. 14) were maintained for many hours as they propagated eastward (the waves are shown at 0900 UTC in Fig. 18b, but they were sustained for 10 h).

5. Sensitivity tests

Figure 19 shows cross sections from the simulation with the same fake-dry configuration but using a “flat”

terrain with a constant height of 1.5 km. Though the cold pool was initially captured, the horizontal thermal difference (density current) dissipated very quickly. The adiabatic cooling from the weak upward motion was far too weak to generate the gravity waves. This further supports our hypothesis that topographical effects were necessary for the generation of the propagating gravity waves.

A totally adiabatic simulation with the same terrain as in the control was also performed. No surface heat flux, latent heat release, or radiative cooling was allowed. Unlike the flat terrain simulation, the gravity waves developed to a large extent similar to the control simulation. The reason for this is because the cold pool, which drives the westward-propagating density current, existed in the initial state just as in the control simulation

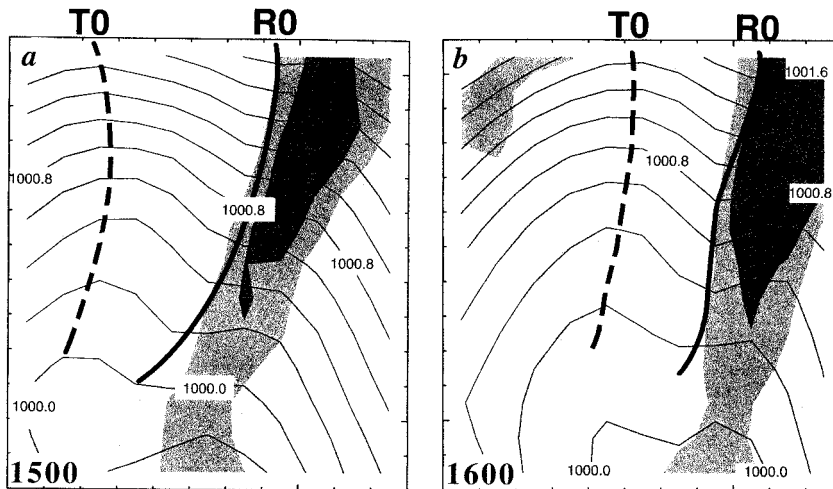


FIG. 17. Model-simulated mean sea level pressure field ($\Delta = 0.2 \text{ hPa}$) and positive vertical motion at 850 hPa (shaded, $\Delta = 3 \text{ cm s}^{-1}$) over approximately the same area as the CCOPE mesonet network at (a) 1500 and (b) 1600 UTC 11 Jul 1981. Gravity wave crest and trough R0 and T0 correspond to those observed in Fig. 2.

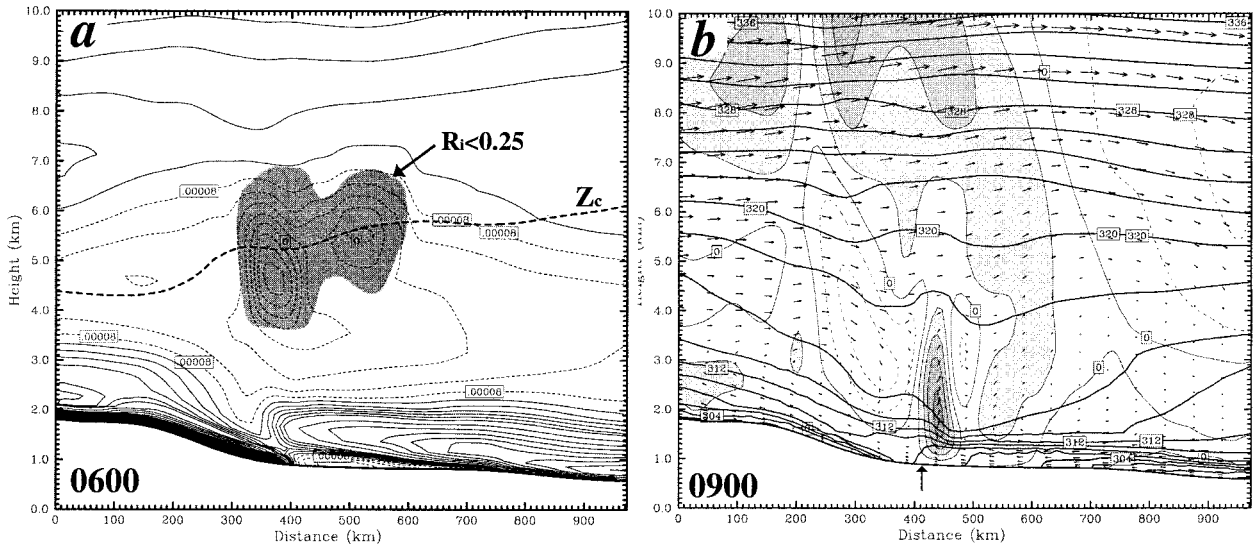


FIG. 18. (a) Vertical cross section of square of moist Brunt-Väisälä frequency (N^2 , $\Delta = 0.00002 \text{ s}^{-1}$, and thin dashed lines indicate $N^2 < 0.0008$). The area shaded indicates Richardson number $Ri < 0.25$ and the thick dashed line shows the wave critical level, assuming a wave speed of 10.2 m s^{-1} . (b) As in Fig. 6 except for 0900 UTC 11 Jul 1981.

and the topographically forced dynamics essential to gravity wave development were present as well.

6. Summary and conclusions

In this paper, the nonhydrostatic PSU-NCAR MM5 version 2 model has been used to investigate orographic gravity wave generation during CCOPE and compared with detailed mesoscale observations. The results of the control simulation show that a series of dynamic and thermodynamic processes at the eastern foothills of the Rocky Mountains generated the first episode of propagating mesoscale gravity waves observed by Koch and Golus (1988). The generation of the gravity waves was

due largely to the low-level local wind system and thermal structure on the eastern slopes (orogenic forcing). Neither wave-CISK (conditional instability of the second kind) (Raymond 1975), nor the geostrophic adjustment and jetogenesis process discussed by Kaplan et al. (1997), generated the waves in the model. The latent heating was suppressed in this simulation, which prohibited wave-CISK. The jet adjustment process in the simulation by Kaplan et al. (1997) produced sizable “mass perturbations” over the lee slopes of the Absaroka Mountains, but they did not share the observed gravity wave characteristics, in particular the fact that they propagated. The simulation presented here clearly shows that lower-tropospheric processes associated with

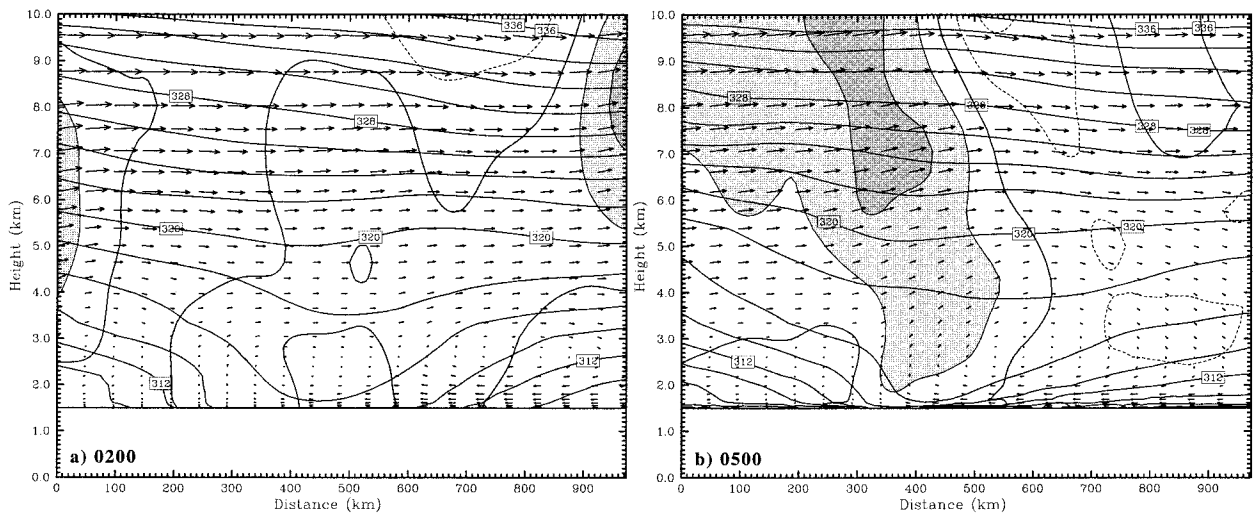


FIG. 19. As in Fig. 6 except from FLAT TERRAIN experiment and for (a) 0200 and (b) 0500 UTC.

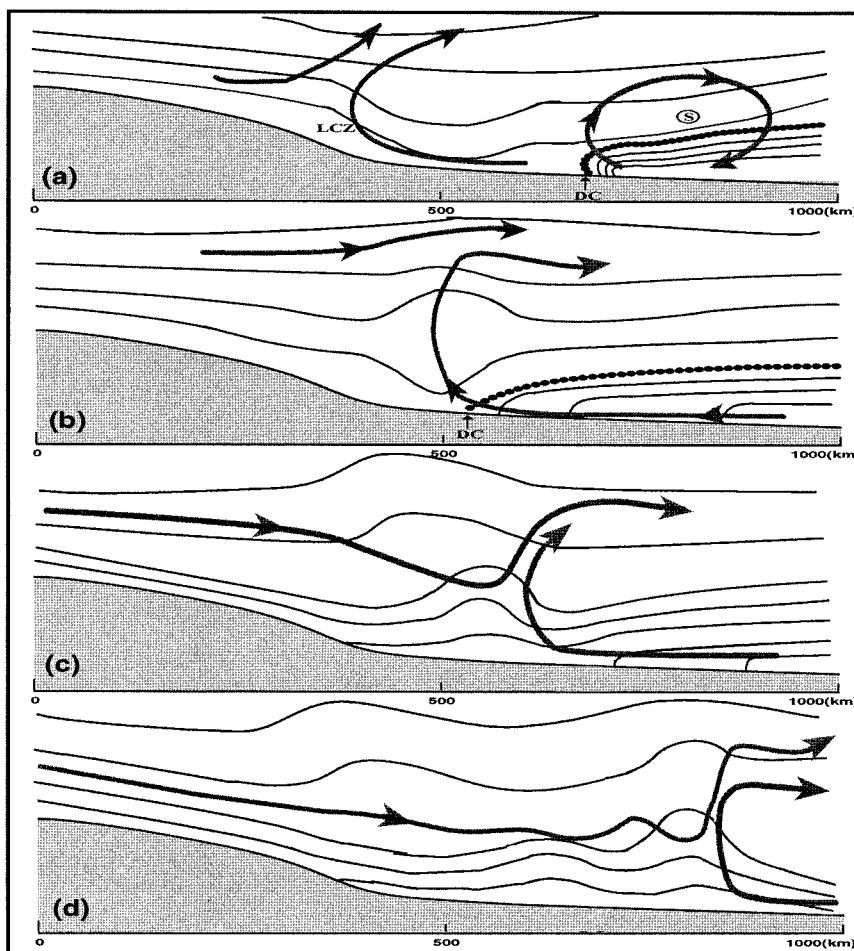


FIG. 20. Schematic multistage wave development conceptual model. (a) Stage 1, westward propagation of remnant MPS in the form of a density current; (b) stage 2, orographic blocking of density current and mesoscale isentropic ridge development in the original lee trough, (c) stage 3, isentropic ridge develops into gravity wave as vertical motions become in quadrature phase with the mass field; and (d) stage 4, mesoscale gravity wave propagates eastward in a well-defined duct. Arrows indicate the relative flows, solid lines show representative isentropes, thick dotted line indicates the density current, and leading edge of the density current (DC) is marked by an arrow. LCZ and center of MPS circulation (S) are also depicted in (a).

a decaying mountain–plains solenoid circulation and an associated retrogressive density current were the agents in gravity wave generation.

A four-stage conceptual model of nighttime gravity wave generation during the summer months over the lee slopes of the Rocky Mountains is presented on the basis of our numerical simulations of the CCOPE case (Fig. 20). The numerical model was initialized slightly before sunset when there was an existing warm lee trough and a downstream MPS with its up-branch along the Montana–North Dakota border and its down-branch situated above a broad cold pool extending to the Great Lakes area.

The first stage is characterized by the up-branch of the remnant daytime MPS (the easternmost convergence zone) being pushed back toward the center of the warm lee trough after sunset (Fig. 20a) by a reversed low-

level pressure gradient force. Near-surface upslope flow advects cooler, denser air from the cold pool region westward toward the leeside convergence zone (LCZ). This circulation system propagates westward as a density current. The cold pool and accompanying MPS subsidence strengthens the low-level inversion necessary for wave ducting during stage 4.

Stage 2 is a transient development (Fig. 20b), in which the westward-propagating density current is blocked at the location of the original warm lee trough just to the east of the steepest slope of the mountain. A mesoscale isentropic ridge gradually forms by adiabatic cooling associated with the strong upward motion at the head of the density current right above the center of the leeside convergence zone. This mass perturbation creates an eastward-directed pressure gradient force, which weakens the flow from the east and hence the original

updraft. In the meantime, a separate upward motion center begins to develop to the east of this cold isentropic ridge due to a shift of the convergence by the opposing pressure gradient force. This is the embryo of the gravity wave.

Stage 3 begins with the appearance of subsidence to the west of the isentropic perturbation (Fig. 20c). Shortly after that, the original low-level updraft associated with the dissipating density current, which created the isentropic ridge, diminishes as the ridge finally cuts off the flow from the east. Thus, the strongest updraft shifts to the east of the mesoscale mass perturbation and a gravity wave develops.

This newly generated gravity wave propagates eastward during stage 4 in a well-defined and extremely efficient duct (Fig. 20d). The gravity wave is first seen in the simulated mean sea level pressure fields a couple of hours after its generation, and displays a timing, location, horizontal wavelength, and pressure–wind phasing quite similar to that observed. The simulated gravity wave persisted for more than 10 h with a wavelength of about 150 km and an average phase speed of $\sim 10.2 \text{ m s}^{-1}$. These characteristics are quite similar to those observed by Koch and Golus (1988), with the exception that the model underestimated the observed phase speed because of an error in the midtropospheric wind forecast near the wave overreflection level.

Though the simulation results presented here argue that the development and evolution of the first gravity wave episode was largely due to processes forced by topography rather than by geostrophic adjustment processes aloft, the synoptic setting fits the Uccellini and Koch (1987) conceptual model well, as described by Koch and Dorian (1988). The upper-level jet still may have played a role in wave forcing, since the imbalance associated with the upper-level jet was not pronounced until 0000 UTC 12 July, which is 12 h after the first wave episode that was investigated in the present study. Also, the upper-level jet is necessary for sustaining the critical layer in the less stable layer above the duct layer.

The process by which an orographically trapped density current can excite the formation of propagating gravity waves is one that may be quite important when a strong mountain–plains solenoid occurs within a highly sheared, stratified flow regime. These results suggest that when conditions necessary for linear gravity wave ducting are present during the summer months over the lee slopes of the Rockies, the mountain–plains circulation may be a prolific producer of mesoscale gravity waves and deep convection hours after the period of diurnal heating has ended.

Acknowledgments. We wish to thank Michael Kaplan, Yuh-Lang Lin, Ronald Weglarz, Yi Jin, Yihua Wu, Michael Trexler, and Lisa Gray for their constructive comments and editorial assistance. Thanks are also extended to the anonymous reviewers for their constructive comments. We also are appreciative of the free software for

analysis of the MM5 output provided by Mark Stoelinga. This research was funded under NSF Grant ATM-9700626. The simulations were performed on the CRAY T916 at the North Carolina Supercomputing Center.

REFERENCES

- Atkinson, B. W., 1981: *Meso-scale Atmospheric Circulations*. Academic Press, 495 pp.
- Banta, R. M., 1984: Daytime boundary-layer evolution over mountainous terrain. Part I: Observations of the dry circulations. *Mon. Wea. Rev.*, **112**, 340–356.
- , 1986: Daytime boundary-layer evolution over mountainous terrain. Part II: Numerical studies of upslope flow duration. *Mon. Wea. Rev.*, **114**, 1112–1130.
- Bischoff-Gauss, I., G. Gross, and F. Wippermann, 1989: Numerical studies on cold fronts. Part II: Orographic effects on gravity flows. *Meteor. Atmos. Phys.*, **40**, 159–169.
- Bossert, J. E., and W. R. Cotton, 1994a: Regional-scale flows in mountainous terrain. Part I: A numerical and observational comparison. *Mon. Wea. Rev.*, **122**, 1449–1471.
- , and —, 1994b: Regional-scale flows in mountainous terrain. Part II: Simplified numerical experiments. *Mon. Wea. Rev.*, **122**, 1472–1489.
- Dudhia, J., 1993: A nonhydrostatic version of Penn State/NCAR mesoscale model: Validation tests and simulation of an Atlantic cyclone and cold front. *Mon. Wea. Rev.*, **121**, 1493–1513.
- Gossard, E. E., and W. H. Hooke, 1975: *Waves in the Atmosphere*. Elsevier, 455 pp.
- Grell, G. A., J. Dudhia, and D. S. Stauffer, 1995: A description of the fifth-generation Penn State/NCAR mesoscale model (MM5). NCAR Tech. Note NCAR/TN-398+STR, 122 pp.
- Jones, W. L., 1968: Reflexion and stability of waves in stably stratified fluids with shear flow: A numerical study. *J. Fluid Mech.*, **34**, 609–624.
- Kaplan, M. L., S. E. Koch, Y.-L. Lin, R. Weglarz, and R. A. Rozumalski, 1997: Numerical simulations of a gravity wave event over CCOPE. Part I: The role of geostrophic adjustment in mesoscale jet streak and gravity wave generation. *Mon. Wea. Rev.*, **125**, 1185–1211.
- Koch, S. E., and P. B. Dorian, 1988: A mesoscale gravity wave event observed during CCOPE. Part III: Wave environment and probable source mechanisms. *Mon. Wea. Rev.*, **116**, 2570–2592.
- , and R. E. Golus, 1988: A mesoscale gravity wave event observed during CCOPE. Part I: Multiscale statistical analysis of wave characteristics. *Mon. Wea. Rev.*, **116**, 2527–2544.
- , and C. O’Handley, 1997: Operational forecasting and detection of mesoscale gravity waves. *Wea. Forecasting*, **12**, 253–281.
- , R. E. Golus, and P. B. Dorian, 1988: A mesoscale gravity wave event observed during CCOPE. Part II: Interactions between mesoscale convective systems and antecedent waves. *Mon. Wea. Rev.*, **116**, 2545–2569.
- , R. Ferrare, S. H. Hefei, W. C. Skillman, and D. Whiteman, 1991: Structure of an internal bore and dissipating gravity current as revealed by Raman lidar. *Mon. Wea. Rev.*, **119**, 857–887.
- , F. Einaudi, P. B. Dorian, S. Lang, and G. M. Heymsfield, 1993: A mesoscale gravity-wave event observed during CCOPE. Part IV: Stability analysis and Doppler-derived wave vertical structure. *Mon. Wea. Rev.*, **121**, 2483–2510.
- Lindzen, R. S., and K. K. Tung, 1976: Banded convective activity and ducted gravity waves. *Mon. Wea. Rev.*, **104**, 1602–1617.
- Pokrandt, P. J., G. J. Tripoli, and D. D. Houghton, 1996: Processes leading to the formation of mesoscale waves in the Midwest cyclone of 15 December 1987. *Mon. Wea. Rev.*, **124**, 2726–2752.
- Powers, J. G., 1997: Numerical model simulations of a mesoscale gravity wave event: Sensitivity tests and spectral analysis. *Mon. Wea. Rev.*, **125**, 1838–1869.
- , and R. J. Reed, 1993: Numerical simulation of the large-am-

- plitude mesoscale gravity-wave event of 15 December 1987 in the central United States. *Mon. Wea. Rev.*, **121**, 2285–2308.
- Raymond, D. J., 1975: A model for predicting the movement of continuously propagating convective storms. *J. Atmos. Sci.*, **32**, 1308–1317.
- Simpson, J. E., 1987: *Gravity Currents: In the Environment and the Laboratory*. John Wiley and Sons, 244 pp.
- , and R. E. Britter, 1980: A laboratory model of an atmospheric mesofront. *Quart. J. Roy. Meteor. Soc.*, **106**, 485–500.
- Smith, R. K., and M. J. Reeder, 1988: On the movement and low-level structure of cold fronts. *Mon. Wea. Rev.*, **116**, 1927–1944.
- Tripoli, G. J., and W. R. Cotton, 1989a: A numerical study of an observed orogenic mesoscale convective system. Part I: Simulation genesis and comparison with observations. *Mon. Wea. Rev.*, **117**, 273–304.
- , and —, 1989b: A numerical study of an observed orogenic mesoscale convective system. Part II: Analysis of governing dynamics. *Mon. Wea. Rev.*, **117**, 305–328.
- Uccellini, L. W., and S. E. Koch, 1987: The synoptic setting and possible source mechanisms for mesoscale gravity wave events. *Mon. Wea. Rev.*, **115**, 721–729.
- Wolyn, P. G., and T. B. McKee, 1994: The mountain–plains circulation east of a 2-km-high north–south barrier. *Mon. Wea. Rev.*, **122**, 1490–1508.